

# Magnetically supramassive and hypermassive compact stars

Kōji Uryū,<sup>1,\*</sup> Shijun Yoshida,<sup>2,†</sup> Eric Gourgoulhon,<sup>3,4,‡</sup> Charalampos Markakis,<sup>5,6,§</sup> Kotaro Fujisawa,<sup>7,¶</sup> Antonios Tsokaros,<sup>8,9,10,\*\*</sup> Keisuke Taniguchi,<sup>1,††</sup> Mina Zamani,<sup>11,‡‡</sup> and Lambros Boukas<sup>12, §§</sup>

<sup>1</sup> Department of Physics, University of the Ryukyus,  
Senbaru 1, Nishihara, Okinawa 903-0213, Japan

<sup>2</sup> Astronomical Institute, Tohoku University, Aramaki-Aoba, Aoba, Sendai 980-8578, Japan

<sup>3</sup>LUX, Observatoire de Paris, Université PSL, CNRS,  
Sorbonne Université, 92190 Meudon, France

<sup>4</sup>Laboratoire de Mathématiques de Bretagne Atlantique,  
CNRS UMR 6205, Université de Bretagne Occidentale,

<sup>6</sup> avenue Victor Le Gorgeu, 29200 Brest, France

<sup>5</sup>Department of Applied Mathematics & Statistics,  
Stony Brook University, Stony Brook, NY 11794, USA

<sup>6</sup>National Center for Supercomputing Applications,  
University of Illinois at Urbana-Champaign, Urbana, IL 61801, USA

<sup>7</sup> Department of Liberal Arts, Tokyo University of Technology,  
5-23-22 Nishi-Kamata, Ota, Tokyo 144-8535, Japan

<sup>8</sup> Department of Physics, University of Illinois Urbana-Champaign, Urbana, IL 61801, USA

<sup>9</sup>National Center for Supercomputing Applications,  
University of Illinois Urbana-Champaign, Urbana, IL 61801, USA

<sup>10</sup>Research Center for Astronomy and Applied Mathematics, Academy of Athens, Athens 11527, Greece

<sup>11</sup> Department of Physics, University of Zanjan, P.O. Box 45195-313, Zanjan, Iran

<sup>12</sup>LAB Scientific Computing Inc., Miami, Florida 33176, USA

(Dated: November 3, 2025)

It is known that the mass of magnetized relativistic compact star is larger than that of non-magnetized one for the same equation of state and central density, albeit the excess of mass is sizable only if the magnetic fields are strong enough  $B \sim 10^{17}-10^{18}$  G. Using our recently developed numerical code COCAL, we systematically compute such compact star solutions in equilibrium associated with mixed poloidal and toroidal magnetic fields, and show the magnetically supramassive solutions whose masses exceed by more than 10% of the maximum mass of the static and spherically symmetric solutions. For some extremely strong magnetic field configurations, we also obtain solutions more massive than the maximum mass of the uniformly rotating solutions at the Kepler (mass-shedding) limit, namely magnetically hypermassive solutions.

PACS numbers:

## I. INTRODUCTION

For a certain equation of state (EOS) of a high density matter, the mass  $M$  of a sequence of solutions of the Tolman-Oppenheimer-Volkov (TOV) equation (a sequence of hydrostatic equilibria in relativistic gravity in static and spherically symmetric spacetime) parametrized by the central density, the  $M(\rho_c)$  curve, exhibits a maximum (see, e.g. [1, 2]). Arguments of a turning point theorem as well as a linear stability analysis prove that the maximum mass is related to the point

of radial instability. Since the maximum mass differs depending on the EOS models, observations of massive neutron stars may rule out the EOS models which cannot support the observed mass (e.g. [3]).

On top of this classic argument for the static and spherically symmetric relativistic stars (TOV solutions hereafter), it is known that the stationary and axisymmetric rapidly rotating relativistic stars may have masses higher than the maximum mass of the TOV solutions (for the same EOS). For the case with uniform rotation [4], the excess of the maximum mass compared to that of TOV-solutions becomes around  $\sim 15 - 20\%$ , and it can be much higher for the cases with differential rotations [5]. The latter differentially rotating solutions are considered as models for the proto neutron stars or the binary neutron star merger remnants [6]. Such uniformly rotating compact stars with the mass higher than the maximum mass of TOV-solutions are called supramassive, and the differentially rotating stars with the mass higher than the maximum mass of the uniformly rotating supramassive solution may be also called hypermassive.

It has been discussed that the maximum mass can be

\*Electronic address: koji.uryu@gmail.com

†Electronic address: yoshida@astr.tohoku.ac.jp

‡Electronic address: eric.gourgoulhon@obspm.fr

§Electronic address: markakis@illinois.edu

¶Electronic address: kotaro.fujisawa@gmail.com

\*\*Electronic address: tsokaros@illinois.edu

††Electronic address: ktngc@cs.u-ryukyu.ac.jp

‡‡Electronic address: m\_zamani@znu.ac.ir

§§Electronic address: lboukas@gmail.com

increased substantially also because of extremely strong magnetic fields (see, e.g. [7]). Therefore, in principle, one can obtain *magnetically supramassive* or *magnetically hypermassive* solutions, whose excess of mass relative to the corresponding unmagnetized solution is due exclusively to the magnetic fields instead of rotation. As such configurations are largely deformed due to the magnetic fields, numerical methods are the most effective approaches to study such solutions. Such magnetically supramassive as well as hypermassive solutions were demonstrated in the very first numerical computations of relativistic stars associated with extremely strong purely poloidal magnetic field [8], closely studied in [9], and also in several calculations under different setups (see, [10] and references therein).

Recently, we have developed a new numerical code for computing equilibria of compact stars associated with mixed poloidal and toroidal magnetic fields as a part of our COCAL code (Compact Object CALculator) [11], [12] (hereafter, Paper I), [13] (Paper II). In our code, exact formulations for the relativistic gravity, the electromagnetic fields, and the hydrostationary equilibria of ideal MHD fluid are incorporated, and are consistently solved numerically. In [11], Papers I and II, we have presented several models of relativistic rotating magnetized stars. Solutions are classified by whether the star is uniformly or differentially rotating, and by whether the outside of the star is electromagnetic vacuum or the force-free magnetosphere. Although we have shown only a couple of solutions for each model, some of the solutions were actually supramassive.

In this paper, extending the computations in Papers I and II, we study the supramassive as well as hypermassive models whose excess of the mass from the maximum mass of TOV solutions are due only to the mixed poloidal and toroidal magnetic fields. Among a few models of such magnetic field configurations, we consider the cases with the compact stars to be associated with an electromagnetic vacuum outside (EMV model), and with a force-free magnetosphere outside (FF model). For the former EMV models, the compact star may or may not contain a force-free toroidal tunnel inside of the star, and its toroidal components should be confined in the stellar interior where the ideal magnetohydrodynamic (ideal MHD) condition is satisfied. For the latter FF model, the toroidal components of the magnetic fields can extend across the interior ideal MHD region to the exterior force-free region (see, Paper II). Since our code computes rapidly rotating magnetized stars, non-rotating magnetized solutions are obtained practically by minimizing the angular velocity parameter. Under the above setups, non-rotating magnetized solutions from lower to higher mass and from weak to extremely strong magnetic fields are systematically calculated. To our knowledge, the COCAL code is unique in calculating such solutions associated with mixed poloidal and toroidal magnetic fields under exact treatments of strong gravity and strong electromagnetism in magneto-hydrostationary equilibrium.

Magnetic fields strong enough to largely deform the stellar configuration can be as extremely high as  $B \sim 10^{18}G$  for a typical compact stars, as such magnetic fields should be close to the virial limit,  $B \sim 10^{18}G(R/10\text{ km})^{-2}(M/M_\odot)$  [7, 14]. This is the magnetic field strength we will see in the interior of our obtained solutions below. So far it is reported that the surface magnetic field of the magnetar candidate of GRB 100625A may be as high as  $\sim 10^{17}\text{ G}$  [15]. It is not only interesting to study such an extremely magnetized star as an astrophysical object in the present universe, such solutions may be useful as initial data of numerical relativity simulations to elucidate the properties of the strong gravitational and electromagnetic effects on the evolution of compact stars (without the effect of rotation) [16].

This paper is organized as follows. In Sec. II, we review a formulation and numerical method developed in our previous works Paper I and II, mentioning that a setting of arbitrary function is modified from the previous works. In Sec. III, we show a sequence of solutions systematically changing the strength of electromagnetic fields as well as the central density. In Sec. IV, we comment some future prospects.

## II. FORMULATION AND NUMERICAL COMPUTATION

In Paper I, the formulation and numerical method for computing stationary and axisymmetric equilibria of strongly magnetized relativistic rotating stars were presented, and in Paper II, they were extended to the case with force-free magnetosphere/magnetotunnel. Full details of our formulation are found in Papers I, II and [17]. Our models and assumptions for the extremely magnetized compact stars are summarized as follows. Hereafter, for index notation for the tensors, the Greek letters  $\alpha, \beta, \dots$  denote 4D objects, the Latin lowercase letters  $a, b, \dots$  spatial 3D objects, and the Latin uppercase letter  $A, B, \dots$  the meridional 2D objects. We use  $G = c = M_\odot = 4\pi\epsilon_0 = 1$  units in this paper unless otherwise specified.

### A. Summary for formulations

The compact star is described by the relativistic ideal magnetohydrodynamic (ideal MHD) fluid, and may (or may not) have a force-free magnetotunnel inside. Outside of the compact star is assumed to be either an electromagnetic vacuum or a force-free magnetosphere, and hence either the ideal-MHD equations (the MHD-Euler equations and the rest mass conservation equation associated with the ideal-MHD conditions), or the force-free conditions are solved simultaneously with Einstein's and Maxwell's field equations. For the field equations, we apply 3+1 decomposition with respect to the foliation of spatial hypersurfaces  $\Sigma$ . Here, we write the 3+1 form of

the metric,

$$ds^2 := -\alpha^2 dt^2 + \gamma_{ab}(dx^a + \beta^a dt)(dx^b + \beta^b dt), \quad (1)$$

where  $\alpha$  and  $\beta^a$  are the lapse and the shift, and  $\gamma_{ab}$  is a restriction of projection tensor  $\gamma_{\alpha\beta} := g_{\alpha\beta} + n_\alpha n_\beta$  to the spatial hypersurface  $\Sigma$ . The hypersurface normal  $n_\alpha$  is defined by  $n_\alpha := -\alpha \nabla_\alpha t$ . We further introduce the conformal decomposition of the spatial metric  $\gamma_{ab} := \psi^4 \tilde{\gamma}_{ab}$ , and separate a flat metric  $f_{ab}$  as  $\tilde{\gamma}_{ab} := f_{ab} + h_{ab}$ .

Under the assumptions of stationarity and axisymmetry, the system of the ideal MHD equations and the force-free conditions are integrated analytically to give a system of first integrals and integrability conditions. We also assume, for simplicity, the flow is homentropic  $s = \text{constant}$ , and circular,  $u^\alpha = u^t(t^\alpha + \Omega \phi^\alpha)$ . Then, the following quantities become arbitrary functions of a potential  $A_\phi$ ,

$$A_t(A_\phi), \quad \Omega(A_\phi), \quad \Lambda(A_\phi), \quad (2)$$

and  $\begin{cases} [\sqrt{-g}\Lambda_\phi](A_\phi) & \text{for ideal MHD,} \\ [\sqrt{-g}B](A_\phi) & \text{for force-free,} \end{cases}$

Here,  $t^\alpha$  and  $\phi^\alpha$  are the timelike and axial Killing vectors, respectively,  $u^\alpha$  is the 4 velocity, and  $\Omega$  the angular velocity. The  $t$  and  $\phi$  components of the electromagnetic 1 form  $A_\alpha$  are written  $A_t = A_\alpha t^\alpha$  and  $A_\phi = A_\alpha \phi^\alpha$ . Functions  $\Lambda(A_\phi)$ , and  $[\sqrt{-g}\Lambda_\phi](A_\phi)$ , are the integrability conditions for  $t$  and  $\phi$  components of MHD-Euler equations, and  $\epsilon^{AB}B := F^{AB}$  is the meridional component of the Faraday tensor,  $F^{\alpha\beta}$ . As discussed in Paper II, the current in the ideal MHD region continues smoothly to the force-free region by choosing a common arbitrary function as

$$\frac{1}{4\pi}[\sqrt{-g}B]'(A_\phi) = [\sqrt{-g}\Lambda_\phi]'(A_\phi), \quad (3)$$

where the prime denotes the derivative with respect to  $A_\phi$ .

Finally, Choices for the EOS and the rotation laws are also a part of integrability conditions. For the EOS, we choose the relativistic polytropic EOS for simplicity,

$$p = K\rho^\Gamma. \quad (4)$$

For the rotation laws, we set the angular velocity  $\Omega(A_\phi)$  to be constant,

$$\Omega(A_\phi) = \Omega_c = \text{constant}, \quad (5)$$

that is, the uniform rotation for EMV model, and to be

$$\Omega(A_\phi) = \Omega_c \Xi'(A_\phi), \quad (6)$$

a differential rotation for FF model, where the function  $\Xi'(A_\phi)$  will be introduced in the next subsection.

Obviously, to study the effect of magnetic fields on the mass of compact stars, it is desirable to calculate solutions with  $\Omega_c = 0$  (strictly non-rotating solutions). To

obtain such solutions, however, a certain modification of our code is necessary. Instead of modifying the code, we use the same magnetized rotating star code developed in our previous works (Paper I, II), and set the parameters of solutions to have  $\Omega_c$  as small as possible,  $\Omega_c \approx 0$ . We will show later that the solutions obtained in this way approximate well the non-rotating models, hence regard them as practically non-rotating solutions.

## B. Assumptions for arbitrary functions

For the above arbitrary functions (2), we choose the same form as in Paper I and II. For EMV models,

$$\Lambda = -\Lambda_0 \Xi(A_\phi) - \Lambda_1 A_\phi - \mathcal{E}, \quad (7)$$

$$A_t = -\Omega_c A_\phi + C_e, \quad (8)$$

$$\sqrt{-g}\Lambda_\phi = \Lambda_{\phi 0} \Xi(A_\phi), \quad (9)$$

$$\sqrt{-g}B = 4\pi \Lambda_{\phi 0} \Xi(A_\phi), \quad (10)$$

where  $\Lambda_0$ ,  $\Lambda_1$ ,  $\mathcal{E}$ ,  $C_e$ , and  $\Lambda_{\phi 0}$  are constant. For FF model, Eq. (8) is replaced by

$$A_t = -\Omega_c \Xi(A_\phi) + C_e. \quad (11)$$

Parameters  $\Lambda_0$ ,  $\Lambda_1$ , and  $\Lambda_{\phi 0}$  are prescribed systematically in order to control the strength of electromagnetic fields from weak, where the solution agrees well with non-magnetized model, to extremely strong where the solutions largely deform. The other constants  $\mathcal{E}$ ,  $\Omega_c$ , and  $C_e$  are calculated from conditions to specify the mass, total angular momentum, and charge of a solution.

Even under the choices of the above relations (7)-(11) for arbitrary functions (2), a form of  $\Xi(A_\phi)$  in each relation can still be chosen arbitrarily (hence differently) under the restriction (3). In Paper I and II, we have used a so called sigmoid function for the derivative  $\Xi'(A_\phi)$  for the all relations for simplicity. In this work, we modify the function  $\Xi'(A_\phi)$  to the fifth degree polynomial which behaves similarly to the sigmoid function as follows,

$$\Xi'(x; b, c) := 6\hat{x}^5 - 5\hat{x}^3 + \frac{15}{8}\hat{x} + \frac{1}{2}, \quad \hat{x} := \frac{x - c}{b}, \quad (12)$$

where  $b$  and  $c$  are parameters satisfying  $0 < b < 1$  and  $0 < c < 1$ . We set this polynomial  $\Xi'(x; b, c)$  monotonically increase from 0 to 1 in an interval  $x \in \left[c - \frac{b}{2}, c + \frac{b}{2}\right] \subset$

$[0, 1]$ .<sup>1</sup> Using this, we set  $\Xi'[A_\phi]$ ,

$$\Xi'(A_\phi) := \begin{cases} 0 & \text{for } \xi \leq -\frac{b}{2}, \\ \Xi'(\xi; b, c) & \text{for } -\frac{b}{2} \leq \xi \leq \frac{b}{2}, \\ 1 & \text{for } \frac{b}{2} \leq \xi, \end{cases} \quad (13)$$

$$\text{where } \xi := \frac{A_\phi - A_\phi^0}{A_\phi^1 - A_\phi^0}. \quad (14)$$

The function  $\Xi'(A_\phi)$  varies from 0 to 1 in an interval  $A_\phi^0 \leq A_\phi \leq A_\phi^1$ . We always set the value of  $A_\phi$  at the rotation axis (z-axis) to be zero. We also set the constant of integration,

$$\Xi(A_\phi) = \int \Xi'(A_\phi) dA_\phi + \text{constant}, \quad (15)$$

to be  $\Xi(0) = 0$ .

In previous Papers I and II, we used a sigmoid function for the arbitrary function  $\Xi'(A_\phi)$ . The new  $\Xi'(A_\phi)$ , Eqs. (13) and (14) defined by the polynomial (12), results in practically the same solutions. We modify  $\Xi'(A_\phi)$  because the sigmoid function does not strictly become 0 or 1 in its asymptotic region.

### C. Model parameters

A solution of magnetized relativistic star is specified with a set of parameters,  $\{\Lambda_0, \Lambda_1, \Lambda_{\phi 0}, \mathcal{E}, \Omega_c, C_e\}$ , appearing in Eqs. (7)-(11), and a set of parameters  $\{A_\phi^0, A_\phi^1, b, c\}$  in the function  $\Xi(A_\phi)$  as Eqs. (12)-(14). The latter set of parameters can be prescribed differently in each  $\Xi(A_\phi)$  appearing in Eqs. (7)-(11) (under a restriction (3), but they are chosen to be the same except for the  $\Xi(A_\phi)$  in differential rotation law (6) (and hence (11)).

For the case of EMV model, the latter set  $\{A_\phi^0, A_\phi^1, b, c\}$  are chosen as in Paper I and II, namely,  $(A_\phi^0, A_\phi^1) = (A_{\phi,S}^{\max}, A_\phi^{\max})$  and  $(b, c) = (0.2, 0.5)$ , where  $A_{\phi,S}^{\max}$  is the maximum value of  $A_\phi$  on the stellar surface, and  $A_\phi^{\max}$  the maximum value of  $A_\phi$  on the stellar support. With the choice  $A_\phi^0 = A_{\phi,S}^{\max}$ , the toroidal component of the magnetic fields is confined inside of the star.<sup>2</sup>

For the case of FF model, the latter set  $\{A_\phi^0, A_\phi^1, b, c\}$  for Eqs.(7), (9), and (10) are chosen as  $(A_\phi^0, A_\phi^1) =$

TABLE I: Quantities at the maximum mass model of Tolman-Oppenheimer-Volkoff (TOV) solutions with the polytropic EOS (4) in  $G = c = M_\odot = 1$  units.  $p_c$  and  $\rho_c$  are the pressure and the rest mass density at the center,  $M_0$  is the rest mass,  $M$  the gravitational mass, and  $M/R$  the compactness (a ratio of the gravitational mass to the circumferential radius). To convert a unit of  $\rho_c$  to cgs, multiply the values by  $M_\odot(GM_\odot/c^2)^{-3} \approx 6.176393 \times 10^{17} \text{ g cm}^{-3}$ .

$\Gamma$	$(p/\rho)_c$	$\rho_c$	$M_0$	$M$	$M/R$
2	0.318244	0.00448412	1.51524	1.37931	0.214440

$(0.3A_{\phi,S}^{\max}, 1.7A_\phi^{\max})$  and  $(b, c) = (1.2, 0.8)$ , and for the rotation law (6) and (11), those are  $(A_\phi^0, A_\phi^1) = (0.0, A_\phi^{\max})$  and  $(b, c) = (0.1, 0.15)$ .

Intensities of the electromagnetic fields inside and outside of the compact stars are controlled by the first three parameters of the former set,  $\{\Lambda_0, \Lambda_1, \Lambda_{\phi 0}, \mathcal{E}, \Omega_c, C_e\}$ . As we have mentioned, we consider non-rotating solutions  $\Omega_c \approx 0$ . The parameter  $C_e$  is evaluated from a condition to vanish the asymptotic charge  $Q$ . The parameter  $\mathcal{E}$  is evaluated from a condition to set a given value for a ratio of the central pressure and density  $(p/\rho)_c$ , which determines the mass of the compact star. Therefore, free parameters in actual computations are  $\{\Lambda_0, \Lambda_1, \Lambda_{\phi 0}, (p/\rho)_c\}$ .

For the polytropic EOS (4), We chose the polytropic index  $\Gamma = 2$ , and the polytropic constant  $K$  to be chosen that the value of  $M_0$  becomes  $M_0 = 1.5$  at the compactness  $M/R = 0.2$  for a spherically symmetric solution in  $G = c = M_\odot = 1$  units. Here,  $M_0$  is the rest mass,  $M$  the gravitational mass, and  $R$  the circumferential radius. The maximum mass model and conversion factors to cgs units are shown in Table I.

### D. Summary for numerical computation

Our numerical method for computing magnetized relativistic stars is detailed in Papers I and II, as well as in our previous papers on a development of COCAL code [18]. A system of equations includes elliptic partial differential equations for the gravitational and the electromagnetic field variables, and algebraic relations for the fluid variables. Those equations are discretized on spherical coordinates, and solved iteratively, writing the elliptic equations in the integral form using the Green's function. The multipole expansion is applied to evaluate the Green's function, where the multipoles whose order is higher than  $L = 60$  are truncated. The resolution of finite difference is set accordingly to resolve the highest multipoles, which is the same as the highest resolution used in Papers I and II. The numbers of grid points and other grid parameters, also used in the present computations, are reproduced in Table II marked as SE3tp.

For a typical run on a workstation, it uses about 40 GB memory, and takes 8.3 min, 12.5 min, and

<sup>1</sup> Note that the derivative of  $\Xi'(x; b, c)$  becomes

$$\partial_x \Xi'(x; b, c) = \frac{30}{b^5} \left( x - c - \frac{b}{2} \right)^2 \left( x - c + \frac{b}{2} \right)^2.$$

<sup>2</sup> In Paper II, we referred this type of solutions with the electromagnetic vacuum outside, with the force-free magnetotunnel, and with the uniform rotation, EV-MT-UR type solutions.

TABLE II: Grid parameters used for computing magnetized rotating compact stars. Normalized radial coordinates  $r_a$ ,  $r_b$ , and  $r_c$  are in the unit of equatorial radius  $R_0$  in the coordinate length.

Type	$r_a$	$r_b$	$r_c$	$N_r^f$	$N_r^m$	$N_r$	$N_\theta$	$N_\phi$	$L$
SE3tp	0.0	$10^6$	1.1	160	176	384	384	72	60
$r_a$ : Radial coordinate where the radial grids starts.									
$r_b$ : Radial coordinate where the radial grids ends.									
$r_c$ : Radial coordinate between $r_a$ and $r_b$ where the radial grid spacing changes.									
$N_r$ : Number of intervals $\Delta r_i$ in $r \in [r_a, r_b]$ .									
$N_r^f$ : Number of intervals $\Delta r_i$ in $r \in [r_a, 1]$ .									
$N_r^m$ : Number of intervals $\Delta r_i$ in $r \in [r_a, r_c]$ .									
$N_\theta$ : Number of intervals $\Delta \theta_j$ in $\theta \in [0, \pi]$ .									
$N_\phi$ : Number of intervals $\Delta \phi_k$ in $\phi \in [0, 2\pi]$ .									
$L$ : Order of included multipoles.									

TABLE III: Parameters of arbitrary functions in the integrability conditions (7)–(10).

Models	$\Lambda_0$	$\Lambda_1$	$\Lambda_{\phi 0}$
EMV <sup>−</sup> I	−2.4	0.24	1.5
EMV <sup>−</sup> II	−3.2	0.32	2.0
EMV <sup>−</sup> III	−4.0	0.40	2.5
EMV <sup>−</sup> IV	−4.8	0.48	3.0
EMV <sup>+</sup>	0.4	0.30–0.567	1.0
FF	4.8	0.30	1.2

16 min, per 1 iteration using a single core of Intel Xeon w5-3525 CPU(3.20GHz), Intel Xeon Platinum 8380 CPU(2.30GHz), and Intel Xeon Gold 6254 CPU(3.10GHz), respectively, and it takes about 600 iterations for a convergence. These systems are fast enough to compute an equilibrium solution or an initial data set on a single time slice, however, it is desirable to speedup the code for systematic computations in a wider parameter range. Recently, parallelized versions of COCAL codes have been developed for (non-magnetized) rotating compact star codes or binary neutron star codes [19], which reached speedups of  $\sim 20$  times faster than the serial code using  $\sim 40$  cores ( $\sim 10$  times faster using  $\sim 20$  cores) on the same kind of workstations as the above. A parallelization of the present magnetized rotating star code is in progress, which is expected to achieve a similar speedup.

### III. RESULTS

#### A. Parameters and caveats for the non-rotating magnetized solutions

Because of the limitation of computing resources, we have investigated only a part of whole parameter space of

the four parameters,  $\{\Lambda_0, \Lambda_1, \Lambda_{\phi 0}, (p/\rho)_c\}$ . From our numerical experiments, we found some combinations of values for magnetic field parameters,  $\{\Lambda_0, \Lambda_1, \Lambda_{\phi 0}\}$ , result in a strong toroidal component comparable to a poloidal one, that is, reproduce solutions associated with mixed poloidal and toroidal fields, so-called “twisted-torus solutions”. We present 3 classes of such solutions, two of which belong to EMV models, and one to FF models. We denote the EMV models as EMV<sup>+</sup> and EMV<sup>−</sup> corresponding to the positive or negative value of the parameter  $\Lambda_0$ , respectively. For the FF model, we will show a model with  $\Lambda_0 > 0$ .

For the EMV<sup>−</sup> models, we systematically change the parameters as tabulated in Table III. The strength of the magnetic fields from weaker to stronger corresponds to EMV<sup>−</sup>I to IV in the Table III. For each EMV<sup>−</sup> model, we set the ratio  $(p/\rho)_c$  to the value of TOV solution to be  $M_0 = 1.25, 1.3, 1.35, 1.4, 1.45, 1.5$  and then  $(p/\rho)_c = 0.3, 0.35, 0.4$ , where  $(p/\rho)_c = 0.3$  is the closest to that of the maximum mass model of TOV solution (see Table I).

As our code is to compute *rotating* magnetized relativistic stars, the ratio of the polar to equatorial radius is used for a parameter to fix the angular velocity  $\Omega_c$ . For a convergence of a solution, the polar radius  $R_z$  and the equatorial radius  $R_0$  are placed on certain grid points of  $z$  and  $x$  coordinates, respectively, and so the ratio can be varied only every  $1/N_r^f$ , where  $N_r^f + 1$  is the number of grid points along the equatorial radius (from the stellar center to the surface). Therefore,  $\Omega_c$  can not be strictly set  $\Omega_c = 0$ , but is set as small as possible in the following computations of (almost) non-rotating solutions.

As we will see below, when the magnetic fields are weak enough as EMV<sup>−</sup>I, solutions with the slowest rotation with  $R_z/R_0 = (N_r^f - 1)/N_r^f$  are obtained which result in our resolution  $\mathcal{T}/|\mathcal{W}| < 10^{-3}$ , where  $\mathcal{T}/|\mathcal{W}|$  is the ratio of the relativistic kinetic to gravitational terms appearing in the relativistic virial relation [20],

$$-\frac{1}{8\pi} \int_{\Sigma} \gamma^{\alpha\beta} (G_{\alpha\beta} - 8\pi T_{\alpha\beta}) dV = 2\mathcal{T} + 3\Pi + \mathcal{M} + \mathcal{W} + M_{\text{ADM}} - M_{\text{K}} = 0, \quad (16)$$

where  $\mathcal{T}$ ,  $\Pi$ ,  $\mathcal{M}$ , and  $\mathcal{W}$ , are kinetic, pressure (internal energy), electromagnetic, and gravitational terms, respectively, whose concrete forms are found in Paper I. As a result of an equality of ADM and Komar masses  $M_{\text{ADM}} = M_{\text{K}}$  [20] for an asymptotically flat spacetime, we have

$$I_{\text{vir}} := |\mathcal{T} + \Pi + \mathcal{M} + \mathcal{W}| = 0. \quad (17)$$

For the EMV<sup>−</sup>II–IV, the equilibrium configurations are substantially deformed. We set  $R_z/R_0$  as small as possible and confirmed that  $\mathcal{T}/|\mathcal{W}| < 2 \times 10^{-3}$  is always satisfied except for a few solutions of FF model which are  $\mathcal{T}/|\mathcal{W}| < 9 \times 10^{-3}$ . In Appendix, we present the physical quantities of selected solutions including the negligible rotation parameters such as the angular velocity and the angular momentum. Among the constructed

non-rotating solutions in this parameter range of EMV<sup>−</sup> models, we found supramassive solutions but not hypermassive solutions.

For the EMV<sup>+</sup> models, we set the parameters to compute from weak to strong magnetic field solutions similarly to EMV<sup>−</sup> models, but change the parameter  $\Lambda_1$  only in the range shown in the Table III. We set the ratio  $(p/\rho)_c$  to the value of TOV solution to be  $M_0 = 1.25, 1.3, 1.35, 1.4, 1.45, 1.5$  and then  $(p/\rho)_c = 0.3$ , and the parameter  $\Lambda_1$  is chosen appropriately depending on the value of  $(p/\rho)_c$  as explained in detail below. Otherwise, we proceed computations the same as EMV<sup>−</sup> models. For a fixed  $(p/\rho)_c$ , as increasing  $\Lambda_1$  the mass of magnetized star increase substantially so that hypermassive solutions are obtained.

Finally for the FF model, we choose only one parameter set shown in the Table III, and set the ratio  $(p/\rho)_c$  to the value of TOV solution to be  $M_0 = 1.25, 1.3, 1.35, 1.4, 1.45, 1.5$  and then  $(p/\rho)_c = 0.3, 0.35, 0.4$ . For this model, magnetically hypermassive solutions are systematically obtained.

In the following, we show as an example the structure of massive solution of such magnetized equilibrium for each EMV<sup>−</sup>, EMV<sup>+</sup> and FF model, then present the solution sequences of magnetically supramassive and hypermassive compact stars.

## B. Solutions of magnetically supramassive and hypermassive compact stars

### 1. Structural comparison of purely magnetized and purely rotating compact stars

In Fig. 1, we show configurations for (non-rotating) magnetically supramassive compact star, model EMV<sup>−</sup>IV, and a uniformly rotating (non-magnetized) supramassive compact star, setting the deformation parameter (the axis ratio in a coordinate length)  $R_z/R_0 = 0.6875$ , and the ratio  $(p/\rho)_c = 0.3$  to be the same for comparison. The uniformly rotating solution is calculated using the COCAL code solving the same waveless formulation under the same coordinate conditions (the maximal slicing and the Dirac gauge conditions) as the magnetized solution.

In all panels of Fig. 1, coordinate lengths ( $x, y, z$ ) are all normalized by the equatorial radius  $R_0$  of the magnetized solution. It is noticed that the size of the non-magnetized rotating solution is about 4.5% larger in coordinate than the magnetized model. In the first row of the Fig. 1, the contours of  $p/\rho$  and its profiles along the  $x$ -axis are shown for the magnetized solution as well as for the rotating solution, and in the second row, the contours of the components of electromagnetic 1-form  $A_t$  and  $A_\phi$ , and the plots of the components of poloidal and toroidal magnetic fields  $B_{\text{pol}} := F_{xy}$  and  $B_{\text{tor}} := -F_{xz}$  are presented. For the same amount of deformation, the magnetized configuration is slightly more compact (that

is, the EOS becomes effectively stiffer) than the rotating one, except for the magnetotunnel region near the equatorial surface where the magnetic fields expel the matter.

For this extremely strong magnetic fields, a qualitative difference can be seen in the metric components. In the bottom row of Fig. 1, contours of the metric components  $h_{xz}$  in  $xz$ -plane, and  $h_{xy}$  in  $xy$ -plane are drawn. Because of the strong magnetic fields near the equatorial surface, the contours for  $h_{xz}$  and  $h_{xy}$  for the magnetized model (the first and second panels from the left of the third row) have more complex structures than those for the rotating model (the third and fourth panels from the left). The density map for the component  $\tilde{\beta}_y$  is also shown in the first and the third panels of the third row ( $xz$ -plane). The effect of magnetic fields does not seem to be large enough to affect this component. Note that because of the lack of significant rotation of the magnetized model,  $\tilde{\beta}_y$  is about an order of magnitude smaller than that of the rotating model.

### 2. Structures of hypermassive solutions

In Fig. 2, we show solutions of magnetically hypermassive compact stars for the EMV<sup>+</sup> and FF models. Model parameters, other than Table III, are set to be  $\Lambda_1 = 0.432$ ,  $(p/\rho)_c = 0.2558203$  ( $M_0 = 1.5$ ), and the axis ratio (in coordinate length)  $R_z/R_0 = 0.7$  for the EMV<sup>+</sup> model, and  $(p/\rho)_c = 0.2558203$  ( $M_0 = 1.5$ ), and  $R_z/R_0 = 0.55$  for FF model. As seen in the contours of  $p/\rho$  and the density profile  $\rho/\rho_c$  along the (normalized)  $x$ -axis, shown in the left and middle panels of the first and second rows, there are toroidal concentrations of matter near the equatorial surface for these solutions with  $\Lambda_0 > 0$  due to extremely strong magnetic fields. This is in contrast with the EMV<sup>−</sup> model ( $\Lambda_0 < 0$ ) that have a force-free tunnel.

A difference between the electromagnetic vacuum and the magnetosphere outside of the star can be seen clearly in the contours of  $A_t$  and  $A_\phi$  in the second and fourth panels of the third row. As mentioned in Paper II, the toroidal components of magnetic fields ought to be confined inside of the star (ideal MHD region) when the outside is the electromagnetic vacuum. For the stars surrounded by the force-free magnetosphere, the toroidal component may or may not cross the surface depending on the choice of arbitrary functions and their parameters. With a choice of parameters discussed in Sec. II C the region of toroidal magnetic field is widely extended across the surface in our FF model as shown in the left and right panels of the second row in Fig. 2.

The mass of EMV<sup>+</sup> and FF models in Fig. 2 are  $M_{\text{ADM}} = 1.6031$  and  $1.8132$ , respectively. The former mass is about 16% above the maximum mass of TOV solution and slightly above the maximum of the uniformly rotating (non-magnetized) star, while the latter is about 31% heavier than the TOV maximum. It is noticed in the right panels of the first and second rows in Fig. 2 that the

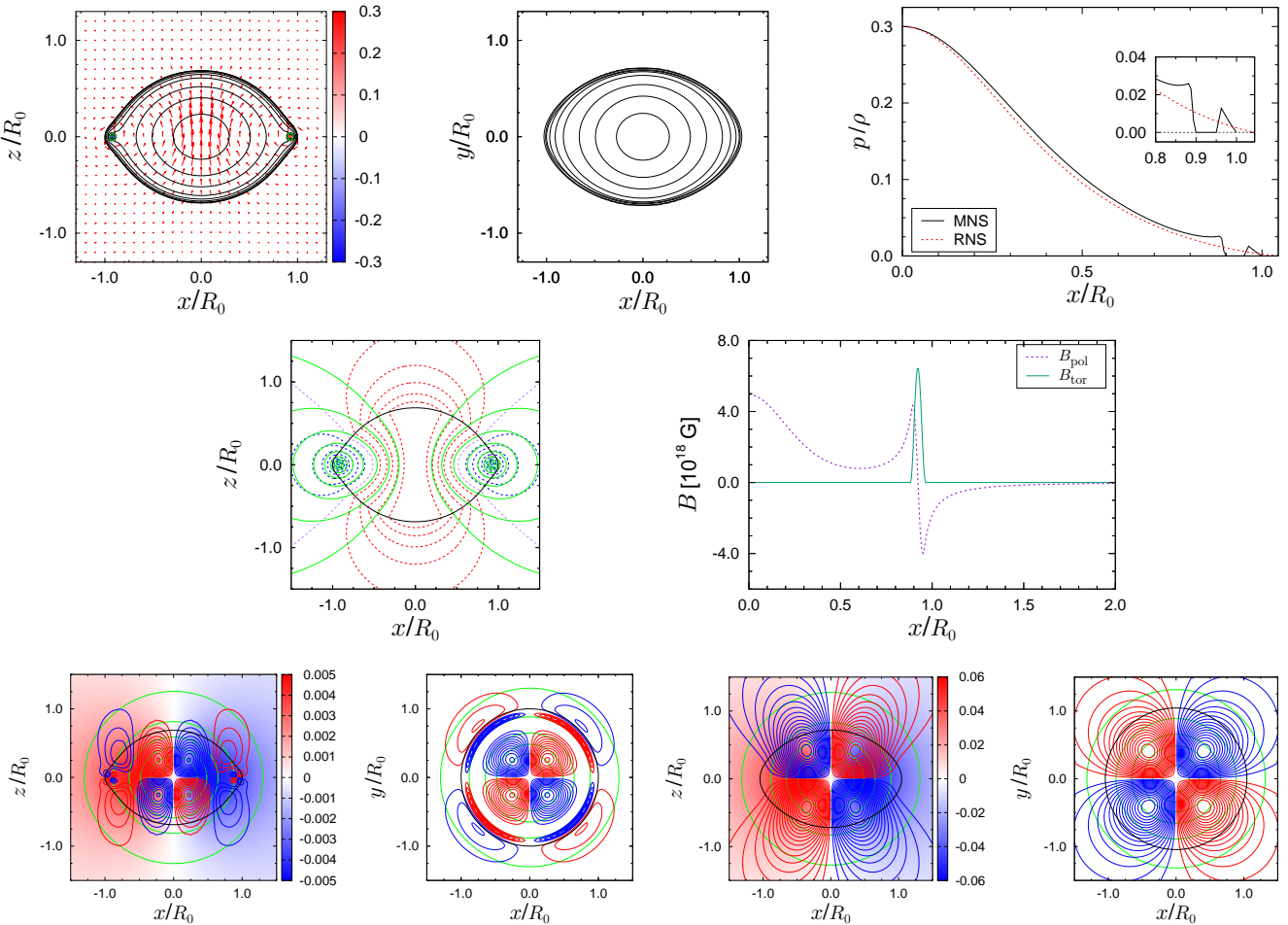


FIG. 1: A (non-rotating) extremely magnetized supramassive compact star associated with mixed poloidal and toroidal magnetic field (EMV<sup>-</sup>IV model) and a uniformly rotating (non-magnetized) compact star are compared for the models with the same axis ratio  $R_z/R_0 = 0.6875$  and the central  $(p/\rho)_c = 0.3$ . First row, left panel: contours of  $p/\rho$  (black closed curves), vector plots of poloidal magnetic field (orange arrows), color density map for the toroidal magnetic fields (red and blue), and the boundary of the magnetotunnel (green circles) for the magnetized star are shown. Middle panel: contours of  $p/\rho$  for the rotating star are shown. The contours are drawn at  $p/\rho = 0.001, 0.002, 0.005, 0.01, 0.02, 0.05, 0.1, 0.2$ . Right panel: the profiles of  $p/\rho$  for both stars are plotted along the normalized equatorial coordinate  $x/R_0$ , and a close-up of the region  $x/R_0 \geq 0.8$  is shown in an inset. Second row, left panel: the contours of the components of electromagnetic 1-form  $A_\phi$  (green curves), the contours of  $A_t$  (dashed red (positive), purple (zero), blue (negative)) are shown for the magnetized star. The black closed curve is the surface of the star. Right panel: components of the magnetic fields,  $B_{\text{pol}} = F_{xy}$  (dashed purple curve) and  $B_{\text{tor}} = -F_{xz}$  (dark green curve) are plotted with respect to the normalized equatorial radius  $x/R_0$ . Third row, left two panels: the metric potentials for the magnetized star in  $xz$  and  $xy$  planes are shown in left and right panels, respectively, which are the contours of  $\psi$  (green closed curves), the color density map for  $\tilde{\beta}_y$  (red and blue), the contours of  $h_{xz}$  (red and blue curves), and the surface of the star (black closed curve). Right two panels: the same as the left two panels but for the uniformly rotating (non-magnetized) star. The coordinate lengths in all panels are normalized by the equatorial radius  $R_0$  of the magnetized star, which is about 4.5% smaller than that of the rotating star.

maximums of the  $B_{\text{pol}}$  and  $B_{\text{tor}}$  of the EMV<sup>+</sup> model are much larger than those of the FF model. The FF model with smaller magnetic field is much heavier because its radius is larger than the EMV<sup>+</sup> model. In proper length, it is  $\tilde{R}_0 = 17.217\text{km}$  for FF model, and  $\tilde{R}_0 = 13.437\text{km}$  EMV<sup>+</sup> model.

### C. Magnetically supramassive and hypermassive solutions

In the top panel of Fig. 3, we show  $M_{\text{ADM}}(p/\rho)_c$  relation for EMV<sup>-</sup>I-IV models. It is confirmed that the mass of strongly magnetized compact stars can exceed the maximum mass of the TOV solutions of the same EOS when the magnetic field and the central  $(p/\rho)_c$  are

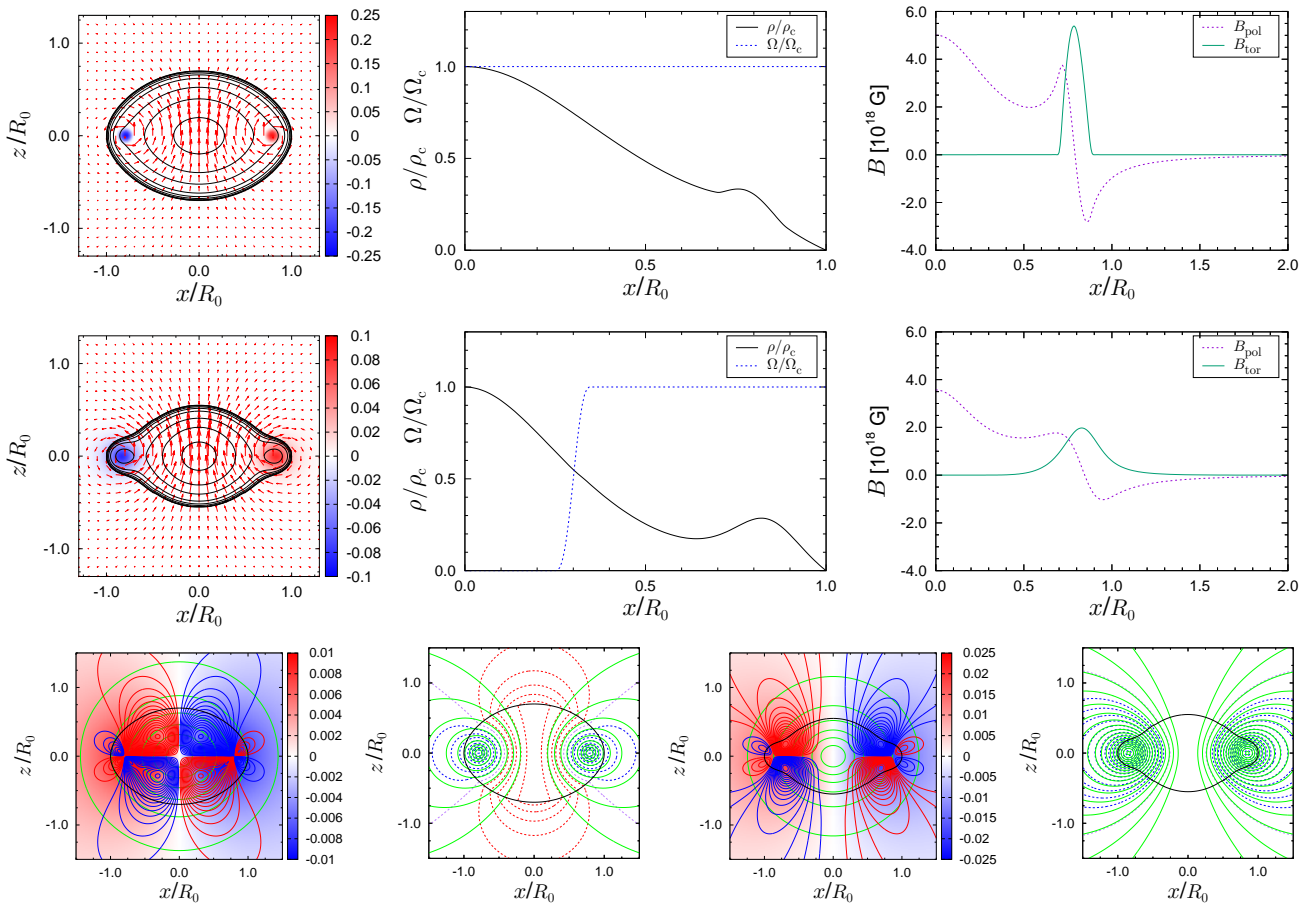


FIG. 2: Solutions for magnetically hypermassive compact stars associated with an electromagnetic vacuum outside (EMV<sup>+</sup> model) and with a force-free magnetosphere outside (FF model). First row: the EMV<sup>+</sup> model with  $\Lambda_1 = 0.432$ ,  $(p/\rho)_c = 0.2558203$  ( $M_0 = 1.5$ ), and  $R_z/R_0 = 0.7$ . Left panel: same as the left panel of the first row of Fig.1. Middle panel: the normalized rest mass density  $\rho/\rho_c$  (red curve) and the normalized angular velocity  $\Omega/\Omega_c$  are plotted along the equatorial radius ( $x$ -axis). Right panel: same as the right panel of the second row of Fig. 1. Second row: the panels are the same as the first row but for the FF model with  $(p/\rho)_c = 0.2558203$  ( $M_0 = 1.5$ ), and  $R_z/R_0 = 0.55$ . Third row: first and second panels from the left are those of the EMV<sup>+</sup> model of the first row, and the third and fourth the FF model of the second row. First panel from left: same as the first (left) panel of the third row of Fig. 1. Second panel: same as the left panel of the second row of Fig. 1. Third and fourth panels: same as the first and the second panels, respectively.

high enough. The excess of mass can be as large as that due to uniform rotation, but its maximum value doesn't surpass that of the maximally rotating (Kepler rotation) model in the selected range of parameters. Therefore, a hypermassive solution is not found for the EMV<sup>-</sup> models within the searched parameter range. Note that EMV<sup>-</sup> models agree very well with the TOV solutions, showing that those solutions with small  $\mathcal{T}/|\mathcal{W}|$  are regarded well as non-rotating solution.

In the bottom panel, we plot the ratio of magnetic to gravitational energy  $\mathcal{M}/|\mathcal{W}|$  with respect to  $(p/\rho)_c$  for the same set of solutions. Their values reach around  $\mathcal{M}/|\mathcal{W}| \sim 0.02 - 0.1$  which are comparable to typical values of  $2\mathcal{T}/|\mathcal{W}|$  of rapidly rotating compact stars (see, Eq. (17)). A value of  $\mathcal{T}/|\mathcal{W}|$  of the compared rotating solution in Fig. 1 is  $\mathcal{T}/|\mathcal{W}| = 0.0419$ , and that of the

maximum mass model with maximal rotation (blue filled circle in the top panel of Fig. 3) is around  $\mathcal{T}/|\mathcal{W}| = 0.050$ , while for the maximum mass model of EMV<sup>-</sup>IV (the one in Fig. 1), the ratio value becomes  $\mathcal{M}/|\mathcal{W}| = 0.11$ .

In Fig.4, we show the  $M-(p/\rho)_c$  plots (top panel) and  $\mathcal{M}/|\mathcal{W}|-(p/\rho)_c$  plots (bottom panel) for EMV<sup>+</sup> and FF models. For EMV<sup>+</sup> models except for  $(p/\rho)_c = 0.3$ , the parameter  $\Lambda_1$  is increased from 0.4–0.55 every 0.05 from bottom to top for each  $(p/\rho)_c$ . In this sequence, it is found that the mass of the solution (and the magnetic fields accordingly) increase rapidly at a certain value of  $\Lambda_1$ . Therefore, at some point, we fix the deformation parameter  $R_z/R_0$  (and  $(p/\rho)_c$ ), then gradually increase the value of  $\Lambda_1$ . The largest  $\Lambda_1$  for each  $(p/\rho)_c$  is  $\Lambda_1 = 0.567, 0.532, 0.491$ , and  $0.432$  for  $(p/\rho)_c = 0.1527579, 0.1733394, 0.2021665, 0.2558203$  ( $M_0 = 1.35$ ,

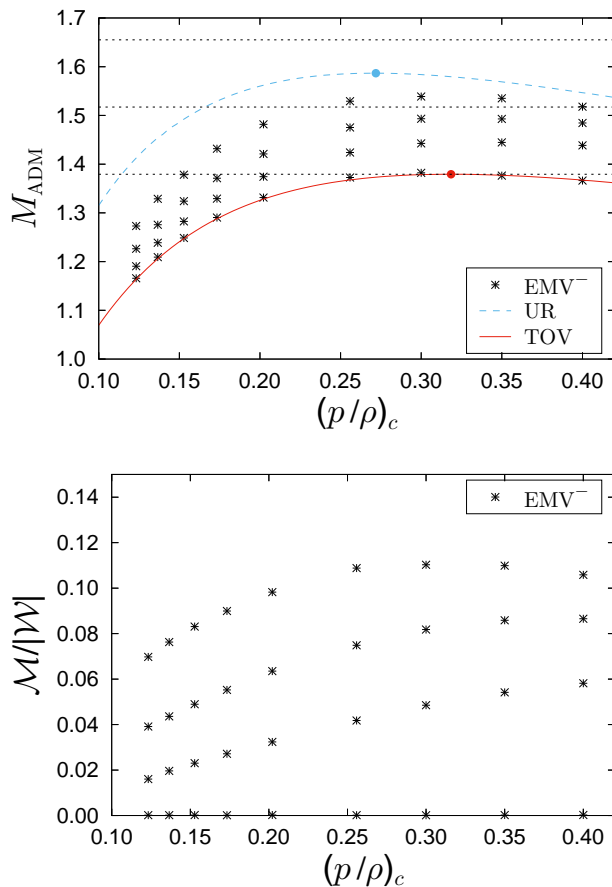


FIG. 3: Sequence of solutions for EMV<sup>-</sup> I-IV models. Top panel: plots of the ADM mass  $M$  with respect to the ratio  $(p/\rho)_c$  of magnetized compact stars (plus-crosses, EMV<sup>-</sup>). A solid (red, TOV) and a dashed (blue, UR) curves correspond, respectively, to the solution sequences of TOV equation and to the maximally rotating (Kepler rotation) models of uniformly rotating relativistic stars with the same EOS. The maximum mass of each curve is shown with a filled circle, and the horizontal dashed lines are drawn at the maximum mass of the TOV solutions and at the 10% and 20% higher values from bottom to top, respectively. Bottom panel: plots of the ratio of magnetic to gravitational energy  $\mathcal{M}/|\mathcal{W}|$  with respect to  $(p/\rho)_c$  for the same EMV<sup>-</sup> I-IV models. In both panels, data points (plus-crosses) from bottom to top at the same  $(p/\rho)_c$  correspond to EMV<sup>-</sup> I-IV models, respectively.

1.4, 1.45, and 1.5), respectively, where the degree of rotation  $\mathcal{T}/|\mathcal{W}|$  becomes the smallest, simultaneously. For  $(p/\rho)_c = 0.3$ , plotted are  $\Lambda_1 = 0.3, 0.35, 0.399$  from bottom to top diamonds. The EMV<sup>+</sup> models with the largest  $\Lambda_1$  at these  $(p/\rho)_c$  ( $M_0 = 1.35, 1.4, 1.45, 1.5$  and  $(p/\rho)_c = 0.3$ ) are the hypermassive solutions.

The caveat is that, for each  $(p/\rho)_c$ , it may be possible to compute a heavier solution associated with stronger magnetic fields for a larger deformation (a smaller value of  $R_z/R_0$ ). Another caveat is that it may also be possible to compute a heavier (and eventually hypermassive)

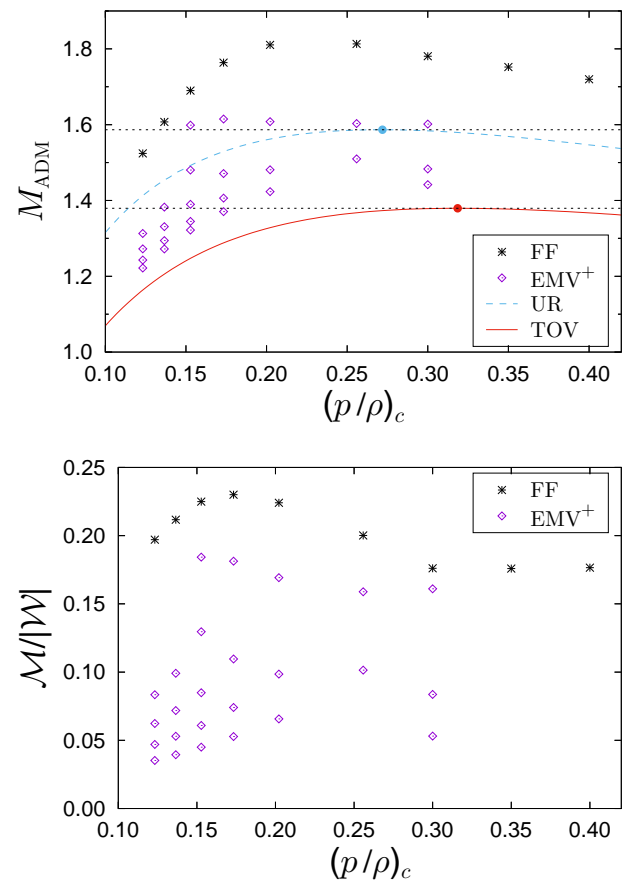


FIG. 4: The same as Fig. 3 but for the EMV<sup>+</sup> (diamonds purple) and FF (plus-crosses) models that include hypermassive solutions. In top panel, the horizontal dashed lines are drawn at values of the maximum mass of the TOV solutions (red) and at the maximum mass of the uniformly rotating solutions (blue).

solution for EMV<sup>-</sup> models applying a similar procedure to change the magnetic field parameters gradually.

For FF model, a sequence of a solutions is obtained systematically from the lower to higher  $(p/\rho)_c$  as plotted also in Fig.4, which are hypermassive except for the lowest  $(p/\rho)_c$  model (with  $M_0 = 1.25$ ). It is noted that the values of  $\mathcal{M}/|\mathcal{W}|$  of these magnetically hypermassive solutions are much larger than  $2\mathcal{T}/|\mathcal{W}|$  of the maximum mass model of rotating star (the blue dot model in the top panel), which is  $2\mathcal{T}/|\mathcal{W}| \approx 0.099$ .

#### IV. DISCUSSION

In the present computation for EMV<sup>-</sup> I-IV in Fig. 1, the excess of the mass of relativistic compact stars only due to the magnetic fields is around  $\sim 12\%$  of the maximum mass of the TOV star. This is comparable but smaller than the excess of the mass due to uniform ro-

tation, which is  $\sim 15\%$  for the  $\Gamma = 2$  EOS. It is not clear that the selected parameter set is close to the limit of strongest magnetic field of such model - a compact star surrounded by electromagnetic vacuum and associated with a force-free tunnel. There is a possibility for computing hypermassive models having stronger magnetic fields than the EMV<sup>-</sup>IV model. It is also possible that hypermassive solution exist with  $\Lambda_0 < 0$  associated with a force-free magnetosphere. The reason for not having proceeded to stronger magnetic field than EMV<sup>-</sup>IV model is solely a lack of computing resources, which may be resolved by the time a parallel version of the code is available.

It is known that various (non-magnetized) differentially rotating solutions become hypermassive as high as  $\sim 20 - 100\%$  depending on the differential rotation models [6]. We found models with  $\Lambda_0 > 0$ , EMV<sup>+</sup> and FF models, can be magnetically hypermassive, and the star become more massive especially when the toroidal region of strong magnetic field near the equatorial surface become wider as in FF model.

As discussed in Sec. III B 1, although the shape of the magnetized neutron star resembles that of a rotating one, its gravitational field such as the magnitude of shift  $\beta_y$  is noticeably different. Therefore for a given shape of a NS, we expect that the effect of frame-dragging will be weaker in a strongly magnetized neutron star, and it may be used as a probe of its magnetic field. In addition, by observing the X-rays emitted from the neutron star's surface the X-ray telescope NICER [28] was able to constrain the neutron star mass-radius relation and the EOS of dense matter. Photons emitted from the star's surface reach an observer by following curved paths that characterize the neutron star's gravitational field which also affects their energy. Similar methodology is also used by the Chandra and XMM-Newton telescopes. Therefore, although a magnetar and a rotating neutron star have similar shapes, their different gravitational fields will lead to different X-ray emissions which in principle may also be used to probe a strong magnetic field.

In [16], we have performed preliminary full GRMHD simulations of such highly magnetized rotating compact stars starting from a selected set of equilibrium solutions obtained from the COCAL code used in the present work. We have found that stability of such highly magnetized rotating compact stars depends strongly on the magnetic field configurations such as the mixture of the toroidal and poloidal components, with some models being highly unstable while others being stable over many Alfvén timescales. Stability of magnetized compact stars is challenging to characterize due to the large pa-

rameter space spanned by magnetized equilibria (which includes density, rotation, magnetic field configuration and strength) (see, e.g. [29, 30]). Further simulations including current magnetically supramassive and hypermassive models as initial data, will shed more light on the properties of these extraordinary compact objects.

### Acknowledgments

This work was supported by JSPS Grant-in-Aid for Scientific Research(C) 22K03636, 18K03624, 25K07274, 18K03606, 24K07053, 21K03556, 20H04728, and NSF Grants No.PHY-2308242 and No.OAC-2310548 to the University of Illinois Urbana-Champaign, and the Marie Skłodowska-Curie grant agreement No.753115. AT acknowledges support from the National Center for Supercomputing Applications (NCSA) at the University of Illinois at Urbana-Champaign through the NCSA Fellows program.

### Appendix A: Physical quantities of selected solutions

In Tables IV–IX, physical quantities of selected solutions for EMV<sup>-</sup>, EMV<sup>+</sup>, and FF models are presented. Those selected solutions are EMV<sup>-</sup>IV model in Tables IV and V, hypermassive solutions of EMV<sup>+</sup> in Tables VI and VII, and solutions of FF model in Tables VI and VII. Definitions of these physical quantities are detailed in Appendix F of Paper I. As explained in Sec. III A, our solutions are approximately non-rotating solutions, which are obtained from our magnetized rotating star code by setting the rotation as small as possible (in practice, maximizing the axis ratio  $R_z/R_0$  under a fixed  $(p/\rho)_c$  for each solution). In the Tables, we also show the rotation related quantities for reference, which are the angular velocity  $\Omega_c$ , the normalized angular momentum  $J/M_{ADM}^2$ , and  $\mathcal{T}/|\mathcal{W}|$ . In the virial relation  $I_{vir} = 2\mathcal{T} + 3\Pi + \mathcal{M} + \mathcal{W} = 0$ , the contribution of kinetic term  $2\mathcal{T}$  is less than 5% (typically around 1%) of the magnetic term  $\mathcal{M}$  and less than 0.4% of the internal energy term  $3\Pi$  for EMV<sup>-</sup> model. For FF model, the contribution of kinetic term  $2\mathcal{T}$  is less than 10% of the magnetic term  $\mathcal{M}$ , and less than 2% of the internal energy term  $3\Pi$ .

As mentioned in Sec. III C, for the hypermassive solutions of EMV<sup>+</sup> models, we further adjust the magnetic field parameter  $\Lambda_1$  to minimize the degree of rotation. Then the contribution of kinetic term  $2\mathcal{T}$  is less than 1.2% of the magnetic term  $\mathcal{M}$ , and less than 0.2% of the internal energy term  $3\Pi$ .

---

[1] J. R. Oppenheimer and G. M. Volkoff, Phys. Rev. **55**, 374-381 (1939); R. C. Tolman, *Relativity, Thermodynamics and Cosmology* (Oxford, 1934);  
[2] S. L. Shapiro and S. A. Teukolsky, “Black holes, white dwarfs, and neutron stars: The physics of compact objects” (Wiley Interscience, New York, 1983)  
[3] J. M. Lattimer, Ann. Rev. Nucl. Part. Sci. **62**, 485 (2012);  
F. Özel and P. Freire, Ann. Rev. Astron. Astrophys. **54**,

TABLE IV: Physical quantities of EMV<sup>-</sup>IV model solutions. Listed quantities are  $(p/\rho)_c$ ,  $\rho_c$ , the equatorial radius in proper length  $\bar{R}_0$ , the ratio of the equatorial to polar radii in the in proper length  $\bar{R}_z/\bar{R}_0$ , the ADM mass  $M_{\text{ADM}}$ , the rest mass  $M_0$ , the proper mass  $M_P$ , the angular velocity  $\Omega_c$ , the angular momentum  $J$ , and a residual of the equality of the Komar mass  $M_K$  and the ADM mass  $M_{\text{ADM}}$ . Units of dimensional quantities are in  $G = c = M_\odot = 1$  unit except for  $\rho_c$  in  $[10^{15} \text{G/cm}^3]$ . To convert a unit of length from  $G = c = M_\odot = 1$  to [km], multiply  $GM_\odot/c^2 = 1.477$  [km] (see, Table I). Details of the definitions for these quantities are found in Appendix F of Paper I.

$(p/\rho)_c$	$\rho_c$	$\bar{R}_0$	$\bar{R}_z/\bar{R}_0$	$M_{\text{ADM}}$	$M_0$	$M_P$	$\Omega_c$	$J/M_{\text{ADM}}^2$	$\mathcal{T}/ \mathcal{W} $	$ 1 - M_K/M_{\text{ADM}} $
0.1232211	1.0717	10.089	0.80475	1.2731	1.3622	1.4434	$3.7872 \times 10^{-3}$	0.073333	$8.2649 \times 10^{-4}$	$1.2125 \times 10^{-5}$
0.1365875	1.1880	10.088	0.78812	1.3289	1.4254	1.5188	$5.9551 \times 10^{-3}$	0.10909	$1.7934 \times 10^{-3}$	$4.2166 \times 10^{-5}$
0.1527579	1.3286	10.019	0.77776	1.3784	1.4815	1.5892	$5.2450 \times 10^{-3}$	0.090385	$1.1968 \times 10^{-3}$	$8.0411 \times 10^{-5}$
0.1733394	1.5076	9.9689	0.76201	1.4317	1.5415	1.6673	$6.7504 \times 10^{-3}$	0.10910	$1.6732 \times 10^{-3}$	$1.0440 \times 10^{-4}$
0.2021665	1.7583	9.8665	0.74720	1.4817	1.5964	1.7460	$6.5455 \times 10^{-3}$	0.098159	$1.2695 \times 10^{-3}$	$2.0349 \times 10^{-4}$
0.2558203	2.2250	9.6580	0.72899	1.5292	1.6439	1.8337	$4.2548 \times 10^{-3}$	0.057361	$3.8256 \times 10^{-4}$	$4.7777 \times 10^{-4}$
0.3000000	2.6092	9.4690	0.72123	1.5387	1.6493	1.8680	$3.7189 \times 10^{-3}$	0.046642	$2.3193 \times 10^{-4}$	$5.5051 \times 10^{-4}$
0.3500000	3.0441	9.2852	0.71365	1.5351	1.6380	1.8854	$6.4798 \times 10^{-3}$	0.076031	$5.6400 \times 10^{-4}$	$7.7099 \times 10^{-4}$
0.4000000	3.4790	9.0859	0.71131	1.5180	1.6126	1.8848	$8.9551 \times 10^{-3}$	0.098861	$8.9010 \times 10^{-4}$	$8.3915 \times 10^{-4}$

TABLE V: Continued from Table IV, listed quantities are the maximum values of poloidal and toroidal magnetic fields,  $B_{\text{pol}}^{\text{max}}$  and  $B_{\text{tor}}^{\text{max}}$ , the ratios of poloidal and toroidal magnetic field energies, and electric field energy, to the total electromagnetic field energy,  $\mathcal{M}_{\text{pol}}/\mathcal{M}$ ,  $\mathcal{M}_{\text{tor}}/\mathcal{M}$ , and  $\mathcal{M}_{\text{ele}}/\mathcal{M}$ , respectively, the ratios of the kinetic, internal, and electromagnetic field energies to the gravitational energy,  $\mathcal{T}/|\mathcal{W}|$ ,  $\Pi/|\mathcal{W}|$ , and  $\mathcal{M}/|\mathcal{W}|$ , respectively, the virial constant divided by the gravitational energy,  $I_{\text{vir}}/|\mathcal{W}|$ , and the electric charge contribution from the volume integral of the star  $Q_M$ . Details of the definitions are found in Appendix F in Paper I. The maximums of magnetic field components  $B_{\text{pol}}^{\text{max}}$  and  $B_{\text{tor}}^{\text{max}}$  are defined by those of spatial Faraday tensor  $F_{ab}$  in Cartesian coordinates,  $B_{\text{pol}} := F_{xy}$  and  $B_{\text{tor}} := -F_{xz}$ . Units of  $B_{\text{pol}}^{\text{max}}$  and  $B_{\text{tor}}^{\text{max}}$  are in [G], and  $Q_M$  in  $G = c = M_\odot = 4\pi\epsilon_0 = 1$  unit.

$B_{\text{pol}}^{\text{max}} \text{[G]}$	$B_{\text{tor}}^{\text{max}} \text{[G]}$	$\mathcal{M}_{\text{pol}}/\mathcal{M}$	$\mathcal{M}_{\text{tor}}/\mathcal{M}$	$\mathcal{M}_{\text{ele}}/\mathcal{M}$	$\Pi/ \mathcal{W} $	$\mathcal{M}/ \mathcal{W} $	$I_{\text{vir}}/ \mathcal{W} $	$Q_M$
$1.1140 \times 10^{18}$	$1.7355 \times 10^{18}$	0.95189	0.047613	0.00049664	0.30964	0.069767	$3.4254 \times 10^{-4}$	$8.3087 \times 10^{-3}$
$1.3320 \times 10^{18}$	$2.0905 \times 10^{18}$	0.94962	0.049140	0.0012389	0.30687	0.076268	$4.6307 \times 10^{-4}$	$1.4851 \times 10^{-2}$
$1.6388 \times 10^{18}$	$2.5257 \times 10^{18}$	0.94837	0.050676	0.00095703	0.30504	0.083080	$5.9062 \times 10^{-4}$	$1.4621 \times 10^{-2}$
$2.0122 \times 10^{18}$	$3.1083 \times 10^{18}$	0.94670	0.051733	0.0015697	0.30245	0.089946	$6.3304 \times 10^{-4}$	$2.1214 \times 10^{-2}$
$2.5966 \times 10^{18}$	$3.8940 \times 10^{18}$	0.94539	0.053168	0.0014468	0.30003	0.098263	$8.7784 \times 10^{-4}$	$2.3309 \times 10^{-2}$
$3.8449 \times 10^{18}$	$5.4580 \times 10^{18}$	0.94443	0.054984	0.00058141	0.29728	0.10881	$1.4214 \times 10^{-3}$	$1.7599 \times 10^{-2}$
$4.9521 \times 10^{18}$	$6.4260 \times 10^{18}$	0.94448	0.055104	0.00041987	0.29690	0.11026	$1.4337 \times 10^{-3}$	$1.6139 \times 10^{-2}$
$6.2841 \times 10^{18}$	$7.5077 \times 10^{18}$	0.94377	0.055026	0.0012012	0.29691	0.10987	$1.7143 \times 10^{-3}$	$2.8945 \times 10^{-2}$
$7.6487 \times 10^{18}$	$8.2906 \times 10^{18}$	0.94351	0.054341	0.0021485	0.29802	0.10585	$1.7019 \times 10^{-3}$	$3.9487 \times 10^{-2}$

TABLE VI: Same as Table IV but for hypermassive solutions of EMV<sup>+</sup> model.

$(p/\rho)_c$	$\rho_c$	$\bar{R}_0$	$\bar{R}_z/\bar{R}_0$	$M_{\text{ADM}}$	$M_0$	$M_P$	$\Omega_c$	$J/M_{\text{ADM}}^2$	$\mathcal{T}/ \mathcal{W} $	$ 1 - M_K/M_{\text{ADM}} $
0.1527579	1.3286	10.180	0.65303	1.5988	1.6982	1.8338	$4.1448 \times 10^{-3}$	$7.5050 \times 10^{-2}$	$6.8280 \times 10^{-4}$	$9.6214 \times 10^{-5}$
0.1733394	1.5076	9.9312	0.66690	1.6149	1.7157	1.8678	$4.8454 \times 10^{-3}$	$8.1499 \times 10^{-2}$	$7.8254 \times 10^{-4}$	$1.2245 \times 10^{-4}$
0.2021665	1.7583	9.5720	0.69319	1.6081	1.7101	1.8802	$5.0466 \times 10^{-3}$	$7.7271 \times 10^{-2}$	$6.8727 \times 10^{-4}$	$1.2398 \times 10^{-4}$
0.2558203	2.2250	9.0977	0.72083	1.6031	1.7015	1.9056	$7.0195 \times 10^{-3}$	$9.4288 \times 10^{-2}$	$9.5463 \times 10^{-4}$	$1.3215 \times 10^{-4}$
0.3000000	2.6092	8.8137	0.72963	1.6016	1.6903	1.9210	$6.6872 \times 10^{-3}$	$8.3190 \times 10^{-2}$	$6.8360 \times 10^{-4}$	$1.5465 \times 10^{-4}$

TABLE VII: Same as Table V, but continued from Table VI for hypermassive solutions of EMV<sup>+</sup> model.

$B_{\text{pol}}^{\text{max}} \text{[G]}$	$B_{\text{tor}}^{\text{max}} \text{[G]}$	$\mathcal{M}_{\text{pol}}/\mathcal{M}$	$\mathcal{M}_{\text{tor}}/\mathcal{M}$	$\mathcal{M}_{\text{ele}}/\mathcal{M}$	$\Pi/ \mathcal{W} $	$\mathcal{M}/ \mathcal{W} $	$I_{\text{vir}}/ \mathcal{W} $	$Q_M$
$2.9720 \times 10^{18}$	$2.8049 \times 10^{18}$	0.93698	0.061975	0.0010454	0.27145	0.18424	$4.7484 \times 10^{-5}$	$1.9958 \times 10^{-2}$
$3.4119 \times 10^{18}$	$3.3710 \times 10^{18}$	0.93272	0.066697	0.00058064	0.27235	0.18129	$1.1263 \times 10^{-4}$	$2.3040 \times 10^{-2}$
$3.9288 \times 10^{18}$	$4.0031 \times 10^{18}$	0.92819	0.071213	0.00059546	0.27645	0.16920	$7.7621 \times 10^{-5}$	$2.2398 \times 10^{-2}$
$5.0105 \times 10^{18}$	$5.3841 \times 10^{18}$	0.92026	0.078673	0.0010673	0.27973	0.15885	$3.7771 \times 10^{-5}$	$2.9312 \times 10^{-2}$
$6.1059 \times 10^{18}$	$6.8819 \times 10^{18}$	0.91487	0.084212	0.00092024	0.27919	0.16102	$3.9331 \times 10^{-5}$	$2.7938 \times 10^{-2}$

TABLE VIII: Same as Table IV but for solutions of FF model.

$(p/\rho)_c$	$\rho_c$	$\bar{R}_0$	$\bar{R}_z/\bar{R}_0$	$M_{\text{ADM}}$	$M_0$	$M_{\text{P}}$	$\Omega_c$	$J/M_{\text{ADM}}^2$	$\mathcal{T}/ \mathcal{W} $	$ 1 - M_{\text{K}}/M_{\text{ADM}} $
0.1232211	1.0717	11.797	0.64346	1.5242	1.6120	1.7032	$4.6195 \times 10^{-3}$	0.10147	$1.4896 \times 10^{-3}$	$1.8156 \times 10^{-4}$
0.1365875	1.1880	11.874	0.62751	1.6073	1.6997	1.8047	$4.7697 \times 10^{-3}$	0.10075	$1.4260 \times 10^{-3}$	$2.0718 \times 10^{-4}$
0.1527579	1.3286	11.949	0.61215	1.6898	1.7854	1.9065	$5.1500 \times 10^{-3}$	0.10443	$1.4784 \times 10^{-3}$	$2.4385 \times 10^{-4}$
0.1733394	1.5076	12.030	0.59778	1.7638	1.8628	2.0026	$7.8792 \times 10^{-3}$	0.15225	$3.0411 \times 10^{-3}$	$3.9391 \times 10^{-4}$
0.2021665	1.7583	11.977	0.59057	1.8104	1.9125	2.0754	$1.0819 \times 10^{-2}$	0.19418	$4.8158 \times 10^{-3}$	$6.0221 \times 10^{-4}$
0.2558203	2.2250	11.657	0.59228	1.8132	1.9178	2.1172	$1.5133 \times 10^{-2}$	0.23687	$6.9993 \times 10^{-3}$	$9.5989 \times 10^{-4}$
0.3000000	2.6092	11.354	0.59769	1.7806	1.8861	2.1114	$1.8779 \times 10^{-2}$	0.26457	$8.7151 \times 10^{-3}$	$1.3012 \times 10^{-3}$
0.3500000	3.0441	10.910	0.60803	1.7521	1.8444	2.0968	$1.5788 \times 10^{-2}$	0.20458	$4.9043 \times 10^{-3}$	$9.2890 \times 10^{-4}$
0.4000000	3.4790	10.521	0.61762	1.7199	1.7969	2.0730	$1.0074 \times 10^{-2}$	0.12196	$1.6377 \times 10^{-3}$	$5.1568 \times 10^{-4}$

TABLE IX: Same as Table V, but continued from Table VIII for solutions of FF model.

$B_{\text{pol}}^{\text{max}} [\text{G}]$	$B_{\text{tor}}^{\text{max}} [\text{G}]$	$\mathcal{M}_{\text{pol}}/\mathcal{M}$	$\mathcal{M}_{\text{tor}}/\mathcal{M}$	$\mathcal{M}_{\text{ele}}/\mathcal{M}$	$\Pi/ \mathcal{W} $	$\mathcal{M}/ \mathcal{W} $	$I_{\text{vir}}/ \mathcal{W} $	$Q_M$
$1.3012 \times 10^{18}$	$8.7929 \times 10^{17}$	0.91363	0.085283	0.0010845	0.26647	0.19707	$5.5045 \times 10^{-4}$	$2.6058 \times 10^{-2}$
$1.5460 \times 10^{18}$	$1.0570 \times 10^{18}$	0.91059	0.088250	0.0011646	0.26163	0.21169	$5.7343 \times 10^{-4}$	$3.0924 \times 10^{-2}$
$1.8508 \times 10^{18}$	$1.2686 \times 10^{18}$	0.90733	0.091307	0.0013654	0.25716	0.22495	$6.1887 \times 10^{-4}$	$3.8143 \times 10^{-2}$
$2.2125 \times 10^{18}$	$1.4796 \times 10^{18}$	0.90285	0.093935	0.0032145	0.25429	0.23003	$1.0062 \times 10^{-3}$	$6.5191 \times 10^{-2}$
$2.6943 \times 10^{18}$	$1.7013 \times 10^{18}$	0.89718	0.096880	0.0059420	0.25495	0.22408	$1.4439 \times 10^{-3}$	$9.4799 \times 10^{-2}$
$3.5689 \times 10^{18}$	$1.9747 \times 10^{18}$	0.88814	0.101067	0.0107966	0.26130	0.20011	$2.0017 \times 10^{-3}$	$1.2954 \times 10^{-1}$
$4.2511 \times 10^{18}$	$2.0837 \times 10^{18}$	0.88139	0.103089	0.0155256	0.26801	0.17606	$2.4641 \times 10^{-3}$	$1.4907 \times 10^{-1}$
$5.3713 \times 10^{18}$	$2.4954 \times 10^{18}$	0.88086	0.109152	0.0099903	0.27096	0.17588	$1.4309 \times 10^{-3}$	$1.2172 \times 10^{-1}$
$6.5857 \times 10^{18}$	$2.9191 \times 10^{18}$	0.88142	0.114841	0.0037342	0.27322	0.17652	$5.4074 \times 10^{-4}$	$7.5347 \times 10^{-2}$

401 (2016); J. M. Lattimer, Ann. Rev. Nucl. Part. Sci. **71**, 433 (2021)

[4] G. B. Cook, S. L. Shapiro and S. A. Teukolsky, Astrophys. J. **422**, 227 (1994) G. B. Cook, S. L. Shapiro and S. A. Teukolsky, Astrophys. J. **424**, 823 (1994)

[5] T. W. Baumgarte, S. L. Shapiro and M. Shibata, Astrophys. J. **528**, L29 (2000); I. A. Morrison, T. W. Baumgarte and S. L. Shapiro, Astrophys. J. **610**, 941 (2004); M. Ansorg, D. Gondek-Rosinska, L. Villain and M. Bejger, EAS Publ. Ser. **30**, 373 (2008);

[6] F. Galeazzi, S. Yoshida and Y. Eriguchi, Astron. Astrophys. **541**, A156 (2012); J. D. Kaplan, C. D. Ott, E. P. O'Connor, K. Kiuchi, L. Roberts and M. Duez, Astrophys. J. **790**, 19 (2014); K. Uryu, A. Tsokaros, F. Galeazzi, H. Hotta, M. Sugimura, K. Taniguchi and S. Yoshida, Phys. Rev. D **93**, no. 4, 044056 (2016); D. Gondek-Rosinska, I. Kowalska, L. Villain, M. Ansorg and M. Kucaba, Astrophys. J. **837**, no. 1, 58 (2017); A. M. Studzinska, M. Kucaba, D. Gondek-Rosinska, L. Villain and M. Ansorg, Mon. Not. Roy. Astron. Soc. **463**, no. 3, 2667 (2016); K. Uryu, A. Tsokaros, L. Baiotti, F. Galeazzi, K. Taniguchi and S. Yoshida, Phys. Rev. D **96**, no. 10, 103011 (2017); A. Bauswein and N. Stergioulas, Mon. Not. Roy. Astron. Soc. **471**, 4956 (2017); G. Bozzola, N. Stergioulas and A. Bauswein, Mon. Not. Roy. Astron. Soc. **474**, no. 3, 3557 (2018); E. Zhou, A. Tsokaros, K. Uryu, R. Xu and M. Shibata, Phys. Rev. D **100**, no. 4, 043015 (2019); A. Passamonti and N. Andersson, Mon. Not. Roy. Astron. Soc. **498**, no. 4, 5904-5915 (2020); X. Xie, I. Hawke, A. Passamonti and N. Andersson, Phys. Rev. D **102**, no. 4, 044040 (2020); P. Iosif and N. Stergioulas, Mon. Not. Roy. Astron. Soc. **503**, no.1, 850-866 (2021); G. Camelio, T. Dietrich, S. Rosswoog and B. Haskell, Phys. Rev. D **103**, no.6, 063014 (2021); P. Iosif and N. Stergioulas, Mon. Not. Roy. Astron. Soc. **510**, no.2, 2948 (2022); K. Franceschetti, L. Del Zanna, J. Soldateschi and N. Bucciantini, Universe **8**, no.3, 172 (2022); M. Cassing and L. Rezzolla, Mon. Not. Roy. Astron. Soc. **532**, no.1, 945 (2024); N. Muhammed, M. D. Duez, P. Chawhan, N. Ghadiri, L. T. Buchman, F. Foucart, P. C. K. Cheong, L. E. Kidder, H. P. Pfeiffer and M. A. Scheel, Phys. Rev. D **110**, no.12, 124063 (2024)

[7] A. G. Suvorov and K. Glampedakis, Phys. Rev. D **105**, no.6, L061302 (2022)

[8] M. Bocquet, S. Bonazzola, E. Gourgoulhon and J. Novak, Astron. Astrophys. **301**, 757 (1995)

[9] C. Y. Cardall, M. Prakash and J. M. Lattimer, Astrophys. J. **554**, 322 (2001)

[10] A. Tsokaros and K. Uryu, Gen. Relativ. Gravit. **54**, 52 (2022).

[11] K. Uryu, E. Gourgoulhon, C. M. Markakis, K. Fujisawa, A. Tsokaros and Y. Eriguchi, Phys. Rev. D **90**, no. 10, 101501(R) (2014)

[12] K. Uryu, S. Yoshida, E. Gourgoulhon, C. Markakis, K. Fujisawa, A. Tsokaros, K. Taniguchi and Y. Eriguchi, Phys. Rev. D **100**, no.12, 123019 (2019), (Paper I)

[13] K. Uryu, S. Yoshida, E. Gourgoulhon, C. Markakis, K. Fujisawa, A. Tsokaros, K. Taniguchi and M. Zamani, Phys. Rev. D **107**, no.10, 103016 (2023), (Paper II)

[14] S. Chandrasekhar and E. Fermi, Astrophys. J. **118**, 116 (1953) [erratum: Astrophys. J. **122**, 208 (1955)]

[15] A. Rowlinson, P. T. O'Brien, B. D. Metzger, N. R. Tanvir and A. J. Levan, Mon. Not. Roy. Astron. Soc. **430**, 1061

(2013)

[16] A. Tsokaros, M. Ruiz, S. L. Shapiro and K. Uryū, Phys. Rev. Lett. **128**, no.6, 061101 (2022) P. C. K. Cheong, A. Tsokaros, M. Ruiz, F. Venturi, J. C. L. Chan, A. K. L. Yip and K. Uryu, Phys. Rev. D **111**, no.6, 063030 (2025)

[17] E. Gourgoulhon, C. Markakis, K. Uryu and Y. Eriguchi, Phys. Rev. D **83**, 104007 (2011)

[18] X. Huang, C. Markakis, N. Sugiyama and K. Uryu, Phys. Rev. D **78**, 124023 (2008); K. Uryu and A. Tsokaros, Phys. Rev. D **85**, 064014 (2012); K. Uryu, A. Tsokaros and P. Grandclement, Phys. Rev. D **86**, 104001 (2012); A. Tsokaros, K. Uryu and L. Rezzolla, Phys. Rev. D **91**, no. 10, 104030 (2015)

[19] L. Boukas, A. Tsokaros and K. Uryu, Universe **10**, no.5, 229 (2024)

[20] E. Gourgoulhon, and S. Bonazzola, Classical and Quantum Gravity, 11, 443 (1994); R. Beig, Physics Letters A, 69, 153 (1978); M. Shibata, K. Uryu and J. L. Friedman, Phys. Rev. D **70**, 044044 (2004) [Erratum-ibid. D **70**, 129901 (2004)]

[21] R. C. Duncan and C. Thompson, Astrophys. J. **392**, L9 (1992); B. Paczynski, Acta Astron. **42**, 145-153 (1992) H. Komatsu, Y. Eriguchi, and I. Hachisu, Mon. Not. Roy. Astron. Soc. **239**, 153 (1989);

[22] For reviews, see e.g., V. M. Kaspi and A. Beloborodov, Ann. Rev. Astron. Astrophys. **55**, 261 (2017); R. Turlolla, S. Zane and A. Watts, Rept. Prog. Phys. **78**, no. 11, 116901 (2015); P. Esposito, N. Rea and G. L. Israel, Astrophys. Space Sci. Libr. **461**, 97-142 (2020)

[23] K. Konno, T. Obata and Y. Kojima, Astron. Astrophys. **352**, 211 (1999). K. Ioka and M. Sasaki, Phys. Rev. D **67**, 124026 (2003); K. Ioka and M. Sasaki, Astrophys. J. **600**, 296 (2004); R. Ciolfi, V. Ferrari, L. Gualtieri and J. A. Pons, Mon. Not. Roy. Astron. Soc. **397**, 913 (2009); R. Ciolfi, V. Ferrari and L. Gualtieri, Mon. Not. Roy. Astron. Soc. **406**, 2540 (2010); S. Yoshida, K. Kiuchi and M. Shibata, Phys. Rev. D **86**, 044012 (2012); S. Yoshida, Phys. Rev. D **99**, no.8, 084034 (2019)

[24] K. Kiuchi, K. Kyutoku, Y. Sekiguchi and M. Shibata, Phys. Rev. D **97**, no. 12, 124039 (2018); R. Ciolfi, W. Kastaun, J. V. Kalinani and B. Giacomazzo, Phys. Rev. D **100**, no. 2, 023005 (2019); M. Ruiz, A. Tsokaros, V. Paschalidis and S. L. Shapiro, Phys. Rev. D **99**, no. 8, 084032 (2019) K. Kiuchi, K. Kyutoku and M. Shibata, Phys. Rev. D **86**, 064008 (2012); P. Mösta *et al.*, Astrophys. J. **785**, L29 (2014); P. Mösta, C. D. Ott, D. Radice, L. F. Roberts, E. Schnetter and R. Haas, Nature **528**, 376 (2015)

[25] K. Glampedakis, S. K. Lander and N. Andersson, Mon. Not. Roy. Astron. Soc. **437**, no. 1, 2 (2014);

[26] A. G. Pili, N. Bucciantini and L. Del Zanna, Mon. Not. Roy. Astron. Soc. **447**, 2821 (2015)

[27] K. Kiuchi and S. Yoshida, Phys. Rev. D **78**, 044045 (2008) J. Frieben and L. Rezzolla, Mon. Not. Roy. Astron. Soc. **427**, 3406 (2012) A. G. Pili, N. Bucciantini and L. Del Zanna, Mon. Not. Roy. Astron. Soc., **439**, 3541 (2014); A. G. Pili, N. Bucciantini and L. Del Zanna, Mon. Not. Roy. Astron. Soc. **470**, no. 2, 2469 (2017)

[28] T. E. Riley, *et al.* Astrophys. J. Lett. **887**, no.1, L21 (2019); G. Raaijmakers, *et al.* Astrophys. J. Lett. **887**, no.1, L22 (2019); A. V. Bilous, *et al.* Astrophys. J. Lett. **887**, no.1, L23 (2019); M. C. Miller, *et al.* Astrophys. J. Lett. **887**, no.1, L24 (2019); S. Bogdanov, *et al.* Astrophys. J. Lett. **887**, no.1, L25 (2019); S. Bogdanov, *et al.* Astrophys. J. Lett. **887**, no.1, L26 (2019)

[29] S. L. Shapiro, Astrophys. J. **544**, 397-408 (2000)

[30] R. J. Tayler, Mon. Not. Roy. Astron. Soc. **161**, 365 (1973); P. Markey, & R. J. Tayler, Mon. Not. Roy. Astron. Soc. **163**, 77 (1973); G. A. E. Wright, Mon. Not. Roy. Astron. Soc. **162**, 339 (1973).